

Reversible and Nonvolatile Manipulation of the Spin-Orbit Interaction in Ferroelectric Field-Effect Transistors Based on a Two-Dimensional Bismuth Oxychalcogenide

Ming-Yuan Yan,^{1,2} Shuang-Shuang Li,³ Jian-Min Yan,⁴ Li Xie,² Meng Xu,⁵ Lei Guo,² Shu-Juan Zhang,³ Guan-Yin Gao,⁶ Fei-Fei Wang^{1,7}, Shan-Tao Zhang,¹ Xiaolin Wang,⁸ Yang Chai^{1,4}, Weiyao Zhao^{1,8,*}, and Ren-Kui Zheng^{2,9,†}

¹*National Laboratory of Solid State Microstructures, College of Engineering and Applied Science & Jiangsu Key Laboratory of Artificial Functional Materials & Collaborative Innovation Center of Advanced Microstructures, Nanjing University, Nanjing 210093, China*

²*State Key Laboratory of High Performance Ceramics and Superfine Microstructure, Shanghai Institute of Ceramics, Chinese Academy of Sciences, Shanghai 200050, People's Republic of China*

³*School of Materials Science and Engineering and Jiangxi Engineering Laboratory for Advanced Functional Thin Films, Nanchang University, Nanchang 330031, People's Republic of China*

⁴*Department of Applied Physics, The Hong Kong Polytechnic University, Hong Kong 999077, People's Republic of China*

⁵*College of Science, Hohai University, Nanjing 211189, People's Republic of China*

⁶*Hefei National Laboratory for Physical Sciences at the Microscale, University of Science and Technology of China, Hefei 230026, People's Republic of China*

⁷*Key Laboratory of Optoelectronic Material and Device, Department of Physics, Shanghai Normal University, Shanghai 200234, People's Republic of China*

⁸*Institute for Superconducting and Electronic Materials, & ARC Centre of Excellence in Future Low-Energy Electronics Technologies, Innovation Campus, University of Wollongong, New South Wales 2500, Australia*

⁹*School of Physics and Materials Science, Guangzhou University, Guangzhou 510006, People's Republic of China*



(Received 3 June 2022; revised 26 August 2022; accepted 29 September 2022; published 28 October 2022)

The spin-orbit interaction (SOI) offers a nonferromagnetic scheme to realize spin polarization through utilizing an electric field. Electrically tunable SOIs through electrostatic gates have been investigated; however, the relatively weak and volatile tunability limits their practical applications in spintronics. Here, we demonstrate the nonvolatile electric field control of the SOI via constructing ferroelectric Rashba architectures, i.e., two-dimensional Bi₂O₂Se/Pb(Mg_{1/3}Nb_{2/3})O₃-PbTiO₃ ferroelectric field-effect transistors. The experimentally observed weak antilocalization (WAL) cusp in Bi₂O₂Se films implies the Rashba-type SOI that arises from the asymmetric confinement potential. Significantly, taking advantage of the switchable ferroelectric polarization, the WAL-to-weak-localization-transition trend reveals the competition between spin relaxation and the dephasing process, and the variation of carrier density leads to a reversible and nonvolatile modulation of the spin-relaxation time and the spin-splitting energy of Bi₂O₂Se films by this ferroelectric gating. Our work provides a scheme to achieve nonvolatile control of the Rashba SOI with the utilization of ferroelectric remanent polarization.

DOI: 10.1103/PhysRevApplied.18.044073

I. INTRODUCTION

The spin-orbit interaction (SOI) has been intensively studied for related exotic physical phenomena and potential applications in spintronic devices and quantum computing fields [1–3]. The SOI may result from either the lack of lattice inversion symmetry, known as the

Dresselhaus effect, or be of Rashba type, with broken-structure symmetry imposed by external fields or an asymmetric confinement potential [4,5]. Unlike traditional magnetic-field-induced spin polarization, the SOI offers a nonferromagnetic scheme to realize the same purpose through utilizing an electric field. The effective modulation of the SOI by an electrostatic field has been explored in low-dimensional systems. However, the tunability of the SOI through these dielectric gates is usually volatile and relatively weak, which is limited by the strength of the

*weiyao.zhao@monash.edu

†zrk@ustc.edu

electric field and low achievable areal charge densities, $n_{2D} \sim 10^{12}\text{--}10^{13} \text{ cm}^{-2}$ [6–8].

Alternatively, ferroelectric materials with large spontaneous electric polarization can generate a strong local electric field and modify the carrier densities of adjacent materials, thus leading to greater tunability [9–11]. Moreover, a ferroelectric gate can potentially tune the spin degree of freedom in a nonvolatile manner, as recently demonstrated in various spintronic devices, such as reversible and nonvolatile electrical switching of spin polarization and spin-charge conversion [12–16]. However, the nonvolatile manipulation of the SOI involves replacing the dielectric gate with a ferroelectric one; this has rarely been reported so far. Thus, it is highly desired to realize the nonvolatile electric field control of the SOI using remanent polarization of ferroelectrics for the development of future spin memory and logic devices.

As an emerging two-dimensional (2D) semiconductor material, the bismuth layered oxyselenide $\text{Bi}_2\text{O}_2\text{Se}$ is a good candidate for the modulation of the SOI; it exhibits superior physical and chemical properties with a moderate band gap (0.8 eV), ultrahigh carrier mobility, and good air stability [17–20]. Recently, some studies have

reported excellent transport properties of $\text{Bi}_2\text{O}_2\text{Se}$, which stimulate the further exploration of its quantum transport phenomena [19,21]. Therefore, it is of great significance to investigate the SOI in the $\text{Bi}_2\text{O}_2\text{Se}$ system, which has been less experimentally studied until now. Moreover, the tetragonal crystal structure ($a = b = 3.89 \text{ \AA}$, $c = 12.21 \text{ \AA}$) of $\text{Bi}_2\text{O}_2\text{Se}$ enables it to be epitaxially grown on the widely used ferroelectric $\text{Pb}(\text{Mg}_{1/3}\text{Nb}_{2/3})\text{O}_3\text{-PbTiO}_3$ (PMN-PT, $a \sim b \sim c \sim 4.02 \text{ \AA}$) single crystal [Fig. 1(a)]. The areal carrier density of $\text{Bi}_2\text{O}_2\text{Se}$ ($n_{2D} \sim 10^{13} \text{ cm}^{-2}$) is lower than that of $n_{2D} \sim 10^{14} \text{ cm}^{-2}$ resulting from the ferroelectric remanent polarization ($P_r \approx 25\text{--}40 \mu\text{C cm}^{-2}$) [10,19,22]. Hence, the 2D $\text{Bi}_2\text{O}_2\text{Se}/\text{PMN-PT}$ heterostructure is a potential candidate system, in which the SOI of $\text{Bi}_2\text{O}_2\text{Se}$ can be reversibly and nonvolatiley manipulated via interfacial polarization charges of ferroelectric PMN-PT.

Here, we achieve nonvolatile manipulation of the SOI through constructing ferroelectric Rashba architectures, i.e., $\text{Bi}_2\text{O}_2\text{Se}/\text{PMN-PT}$ 2D ferroelectric field-effect transistors (FEFETs) [Fig. 1(b)]. Different from tuning the interfacial spin-orbit coupling with ferroelectricity through the spin Hall angle [23], this work demonstrates SOI tuning in the $\text{Bi}_2\text{O}_2\text{Se}/\text{PMN-PT}$ heterostructure by a

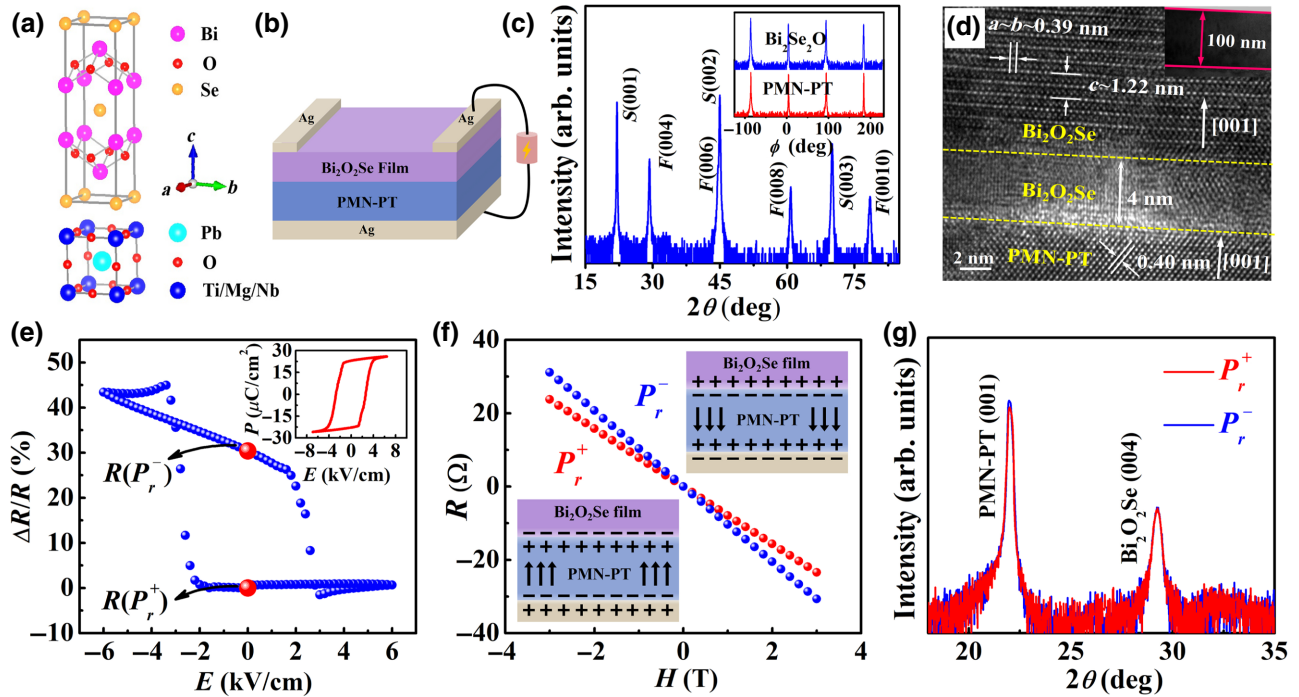


FIG. 1. (a) Crystal structure of tetragonal $\text{Bi}_2\text{O}_2\text{Se}$ and pseudocubic PMN-PT. (b) Schematic diagram of the $\text{Bi}_2\text{O}_2\text{Se}/\text{PMN-PT}$ 2D FET device. (c) XRD θ - 2θ scan and ϕ -scan patterns (inset) for the $\text{Bi}_2\text{O}_2\text{Se}/\text{PMN-PT}$ heterostructure. Here, F and S represent the $\text{Bi}_2\text{O}_2\text{Se}$ film and PMN-PT substrate, respectively. (d) TEM image taken on the interface of 100-nm $\text{Bi}_2\text{O}_2\text{Se}/\text{PMN-PT}$. (e) Relative resistance change ($\Delta R/R$) of the 75-nm $\text{Bi}_2\text{O}_2\text{Se}$ film as a function of electric field, E , applied to PMN-PT; inset shows ferroelectric polarization versus electric field (P - E) loop of PMN-PT (001). (f) Room-temperature Hall resistance of the 75-nm $\text{Bi}_2\text{O}_2\text{Se}$ film versus magnetic field when PMN-PT is in the positive (P_r^+) and negative (P_r^-) poled states, respectively, and schematic illustration of the accumulation of negative (bottom-left inset) and positive (top-right inset) polarization charges under P_r^+ and P_r^- states of PMN-PT. (g) XRD θ - 2θ scan pattern of the $\text{Bi}_2\text{O}_2\text{Se}$ film for the P_r^+ and P_r^- states of PMN-PT.

magnetotransport method. Upon switching the direction of ferroelectric polarization, the *in situ* electric field control of carrier density, resistance, and magnetoresistance are realized by the ferroelectric field effect. Further magnetotransport measurements demonstrate the presence of a Rashba-type SOI in $\text{Bi}_2\text{O}_2\text{Se}$ films arising from the asymmetric confinement potential. The dependence of the weak antilocalization (WAL) to weak localization (WL) transition on polarization state, thickness, and temperature reveal that the crossover is determined by the relative scale of the spin-relaxation length and the phase-coherence length. Moreover, utilizing the ferroelectric gate, the SOI and the spin-splitting energy can be modulated in a reversible and nonvolatile manner.

II. EXPERIMENTS

$\text{Bi}_2\text{O}_2\text{Se}$ films are deposited on (001)-oriented PMN-PT single-crystal substrates by pulsed laser deposition with a XeCl excimer laser ($\lambda = 308$ nm). Before the deposition of films, the base pressure of the chamber is evacuated to a pressure lower than 5.0×10^{-5} Pa. The working pressure is maintained at 3.0×10^{-3} Pa during the film-deposition process. Other preparation parameters, like the target-to-substrate distance, laser energy density, substrate temperature, and pulse repetition rate, are kept at 6 cm, 2 J cm^{-2} , 400°C , and 3 Hz, respectively. After the completion of deposition, the as-grown films are cooled naturally to room temperature.

Ag electrodes with a thickness of 100 nm are deposited on the top surface of $\text{Bi}_2\text{O}_2\text{Se}$ films and the whole back of the bottom of PMN-PT substrates. The top Ag electrodes with different sizes are used to measure the electrical resistance and Hall resistance (Fig. S1 within the Supplemental Material [24]), respectively. The bottom Ag electrode together with one top Ag electrode are used to apply an electric field to switch the polarization direction of the PMN-PT substrates.

The phase purity, out-of-plane and in-plane orientations, and crystallinity of the grown films are analyzed by using an x-ray diffractometer (PANalytical X'Pert PRO) equipped with Cu $K\alpha_1$ radiation ($\lambda = 1.5406 \text{ \AA}$). The crystal structure and interface epitaxy of the prepared heterostructures are also characterized using a transmission electron microscope (Tecnai G2 F20 S-Twin). The surface morphology of $\text{Bi}_2\text{O}_2\text{Se}$ films and the piezoelectric properties of PMN-PT substrates are characterized by atomic force microscopy (AFM) and piezoresponse force microscopy (PFM) using an atomic force microscope (MFP-3D, Asylum Research Inc.) The polarization-electric field (P - E) hysteresis loops of PMN-PT substrates are recorded by means of a TF3000 ferroelectric analyzer (aiXACCT, Germany) at room temperature. The electronic transport properties of $\text{Bi}_2\text{O}_2\text{Se}$ films, including the resistance, magnetoresistance, and carrier density,

are measured via the standard four-probe technique and the van der Pauw method, respectively, using a physical property measurement system (Quantum Design).

III. RESULTS AND DISCUSSION

The x-ray diffraction (XRD) θ - 2θ scan pattern in Fig. 1(c) shows that (00*l*)-oriented ($l = 4, 6, 8, 10$) diffraction peaks are detected for the $\text{Bi}_2\text{O}_2\text{Se}$ film, implying that the film is single phase and *c*-axis oriented. The XRD rocking curve taken on the $\text{Bi}_2\text{O}_2\text{Se}$ (004) diffraction peak yields a full width at half maximum of 0.93° (Fig. S2 within the Supplemental Material [24]), indicating that the $\text{Bi}_2\text{O}_2\text{Se}$ film has a relatively high degree of crystallinity. The homogeneous distribution of Bi, O, and Se elements (Fig. S3 within the Supplemental Material [24]) and a relatively smooth surface with a root-mean-square roughness of 4.5 nm shown by the AFM image [Fig. S4(a) within the Supplemental Material [24]] further suggest the good quality of the $\text{Bi}_2\text{O}_2\text{Se}$ film. As depicted by the azimuthal ϕ scans in the inset of Fig. 1(c), the film and substrate both show fourfold symmetry, which reveals that the $\text{Bi}_2\text{O}_2\text{Se}$ film grows epitaxially on the PMN-PT substrate. In addition, the epitaxial relationship is further confirmed by the HRTEM image. As shown in Fig. 1(d), a $\text{Bi}_2\text{O}_2\text{Se}$ buffer layer about 4 nm thick is formed near the interface, and then the film grows layer by layer along the *c* axis. The formation of the buffer layer is probably caused by the smaller lattice constant of $\text{Bi}_2\text{O}_2\text{Se}$ ($a \sim b \sim 0.39 \text{ nm}$) than that of PMN-PT ($a \sim b \sim c \sim 0.40 \text{ nm}$), to release the tensile strain accumulated at the beginning of film deposition. Afterwards, the lattice spacings of 0.39 and 1.22 nm correspond to the lattice parameters *a* (*b*) and *c* of the $\text{Bi}_2\text{O}_2\text{Se}$ unit cell, which manifests the well-defined atomic arrangement and epitaxial growth of the $\text{Bi}_2\text{O}_2\text{Se}$ film.

The superior ferroelectric properties of the PMN-PT (001) substrate are illustrated by the complete PFM images [Figs. S4(b)–S4(d) within the Supplemental Material [24]]. The shape of the $\Delta R/R$ versus *E* curve in Fig. 1(e) is similar to that of the *P*-*E* loop of PMN-PT [inset of Fig. 1(e)], implying that the ferroelectric field effect determines the resistance-switching behavior. Here, $\Delta R/R$ is defined as $\Delta R/R = [R(E) - R(0)]/R(0)$, where *R*(*E*) and *R*(0) are the resistance of the film with and without the application of external electric fields, respectively. After removing the electric field, a maximum value of about 30% $\Delta R/R$ is achieved for a 75-nm $\text{Bi}_2\text{O}_2\text{Se}$ film as the polarization state changes from P_r^- to P_r^+ at room temperature, where P_r^- and P_r^+ states represent the negative [top-right inset in Fig. 1(f)] and positive [bottom-left inset in Fig. 1(f)] polarization states of the PMN-PT substrate, respectively. Notably, the resistance-relaxation behavior manifested by the nonsquare $\Delta R/R$ versus *E* curve [Fig. 1(e)] can be caused by the trapping effects of defect states in the 4-nm disordered interfacial layer [25].

The negative Hall coefficients in Fig. 1(f) show that the 75-nm $\text{Bi}_2\text{O}_2\text{Se}$ film is an n -type semiconductor, the majority charge carriers of which are electrons. The correspondingly calculated room-temperature carrier densities, n , are $1.06 \times 10^{19} \text{ cm}^{-3}$ for the P_r^+ state and $0.81 \times 10^{19} \text{ cm}^{-3}$ for the P_r^- state. In addition, the *in situ* XRD θ - 2θ scan in Fig. 1(g) proves that the polarization reversal of PMN-PT does not affect the strain state of the film, since the diffraction peaks of the $\text{Bi}_2\text{O}_2\text{Se}$ film remain unchanged. All this evidence confirms that the resistance change of the $\text{Bi}_2\text{O}_2\text{Se}$ film is dominated by the ferroelectric field effect. As schematically illustrated by the bottom-left inset in Fig. 1(f), with the PMN-PT positively poled, the negative polarization charges will appear at the top surface of the PMN-PT substrate. These negative polarization charges will attract hole carriers in the film to the interface region. This results in an increase in the electron carrier density of the film, and thus, a decrease in the resistance of the film. The situation for the P_r^- state

is opposite by applying a negative electric field to PMN-PT [top-right inset in Fig. 1(f)]. Consequently, the nonvolatile and reversible modulation of resistance and carrier density are realized in $\text{Bi}_2\text{O}_2\text{Se}/\text{PMN-PT}$ 2D FEFETs.

The low-temperature electronic transport properties of $\text{Bi}_2\text{O}_2\text{Se}$ films with several representative thicknesses are studied. With decreasing film thickness, the measured volume carrier density decreases monotonously, as shown in Fig. 2(a), and the discrepancy in the carrier density between the P_r^+ and P_r^- states becomes more pronounced. This suggests the more-prominent modulation ability of the ferroelectric field effect as the films become thinner, which is consistent with the largest $\Delta R/R$ realized for the 75-nm film (Fig. S5 within the Supplemental Material [24]). On the other hand, the values of the Ioffe-Regel parameter, $k_F l = (3\pi^2 n)^{2/3} \hbar \mu / e$, where \hbar is the reduced Planck constant and μ is the electron mobility (Fig. S6 within the Supplemental Material [24]), for different film thicknesses are obviously larger than that at

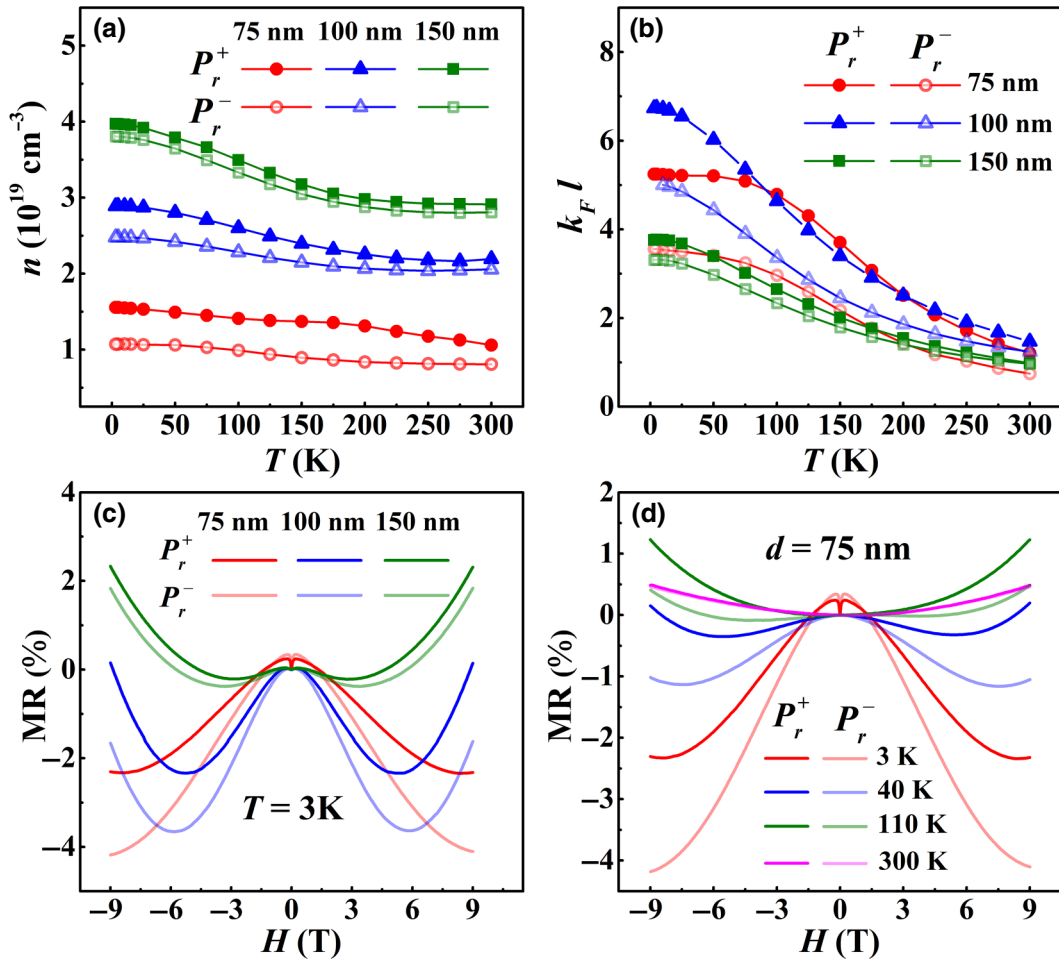


FIG. 2. (a) Temperature dependence of the carrier density of $\text{Bi}_2\text{O}_2\text{Se}$ films with different thicknesses. (b) Temperature dependence of the Ioffe-Regel parameter ($k_F l$) of $\text{Bi}_2\text{O}_2\text{Se}$ films with different thicknesses. (c) Magnetic-field-dependent MR of $\text{Bi}_2\text{O}_2\text{Se}$ films with different thicknesses at 3 K. (d) Magnetic-field-dependent MR of the 75-nm $\text{Bi}_2\text{O}_2\text{Se}$ film at various fixed temperatures.

low temperature of about 200 K [Fig. 2(b)], implying that Bi₂O₂Se films are in the weakly disordered regime at this temperature range [26,27].

The magnetoresistance (MR) of the Bi₂O₂Se films in Fig. 2(c) exhibits a polarization-induced difference and shows a similarly reduced magnitude of regulation with increasing film thickness. Here, MR is defined as $\text{MR} = [R(H) - R(0)]/R(0)$, where $R(H)$ and $R(0)$ refer to the resistance in the presence and absence of a magnetic field, H , respectively. As the film thickness increases, in the range of $H > 1$ T, the shape of the MR varies from a parabola pointing downwards to a double-dip W-shaped curve, finally to a parabola pointing upwards, along with the sign changing from negative to positive. This transition behavior of MR, including the sign and magnitude, is strongly influenced by different carrier densities [28,29]. On the other hand, the MR of the 75-nm Bi₂O₂Se film with increasing temperature in Fig. 2(d) and Figs. S7–S9 within the Supplemental Material [24] resembles the curve-shaped transitions mentioned above. Particularly, a sharp cusp near zero magnetic field in the MR curve is observed at low temperatures. This is a characteristic signature of the WAL effect, which implies the presence of the SOI in the Bi₂O₂Se films.

As an effective method to identify the SOI, the low-field magnetoconductance behavior due to WL and WAL are extensively employed to investigate spin-relaxation processes in various systems [30]. For a 2D disordered system, the low-field WAL effect with different mechanisms can be described by the Iordanskii-Lyanda-Geller-Pikus (ILP) theory [see Eq. (S1) within the Supplemental Material [24]] or the Hikami-Larkin-Nagaoka (HLN) theory [31,32]. As the assumption is satisfied from the Ioffe-Regel parameter, $k_F l > 1$, the fittings of low-field magnetoconductance, $\Delta G = G(H) - G(0) = R^{-1}(H) - R^{-1}(0)$, with both theories are shown in Fig. 3. It is clear that the HLN fitting provides better agreement with the experimental data (see Table S1 within the Supplemental Material [24]), proving that the HLN theory is more effective for describing WAL in the Bi₂O₂Se film, which is consistent with the earlier literature [33]. Specially, the magnetoconductance of the WAL effect using HLN theory is given as

$$\begin{aligned} \Delta G(B) = & -\frac{e^2}{\pi h} \left[\frac{1}{2} \psi \left(\frac{B_\phi}{B} + \frac{1}{2} \right) - \frac{1}{2} \ln \left(\frac{B_\phi}{B} \right) \right. \\ & + \psi \left(\frac{B_{so} + B_{el}}{B} + \frac{1}{2} \right) - \ln \left(\frac{B_{so} + B_{el}}{B} \right) \\ & - \frac{3}{2} \psi \left(\frac{(4/3)B_{so} + B_\phi}{B} + \frac{1}{2} \right) \\ & \left. + \frac{3}{2} \ln \left(\frac{(4/3)B_{so} + B_\phi}{B} \right) \right]. \end{aligned} \quad (1)$$

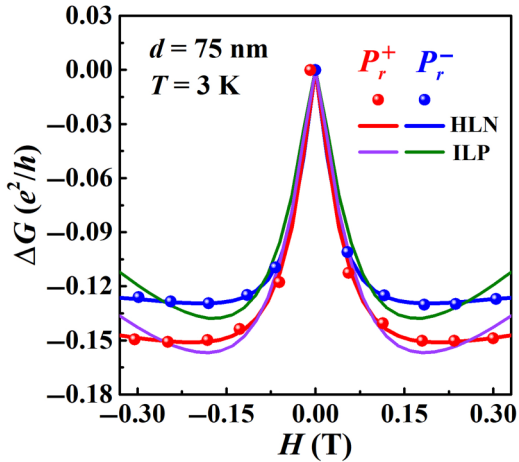


FIG. 3. Experimental WAL data of the 75-nm Bi₂O₂Se film for the P_r^+ and P_r^- states of PMN-PT, as measured at $T = 3$ K. Solid lines are fitted with different theories (red and blue lines for the HLN theory, purple and green lines for the ILP theory).

Here, Ψ is the digamma function. The three subscripts, φ , so , and el , denote the inelastic dephasing process, spin-orbit scattering, and elastic scattering, respectively. The characteristic magnetic fields, B_φ , B_{so} , and B_{el} , can be extracted from the fitting to experimental data. The mean free path, $L_{el} = (\hbar/4eB_{el})^{1/2}$ (Fig. S12 within the Supplemental Material [24]), is much smaller than the distance between the two top electrodes, and thus, carrier transport in the Bi₂O₂Se films is in the diffusive regime [33].

To determine the strength of the SOI, the low-field ΔG values of the 75-nm Bi₂O₂Se film for the P_r^+ and P_r^- states are fitted and plotted in Fig. 4(a) for the most notable WAL feature, and other ΔG data of films with different thicknesses are shown in Figs. S10 and S11 within the Supplemental Material [24]. At $T = 3$ K, the observed sharp WAL peak of ΔG near zero field is caused by the positive correction to the conductance with the presence of the SOI. With heating to 30 K, the sharp peak is gradually suppressed and eventually develops into a broad dip, which is a signature of the WL effect. Hence, the temperature-dependent WAL-WL transition is observed here, as reported in previous trilayer graphene, SrTiO₃ FETs, and the InAs/GaSb double quantum well [34–36]. Intriguingly, upon ferroelectric polarization switching from the P_r^+ state to the P_r^- state of the PMN-PT substrate, the WAL effect is suppressed, as reflected by the decrease in the magnitude of ΔG and a broadening of the WAL peak of the Bi₂O₂Se film, exhibiting a polarization-induced tendency from WAL to WL.

To investigate the spin-relaxation and phase-coherence processes, the temperature-dependent spin-relaxation length, L_{so} , and the dephasing length, L_φ , calculated from $L_{so,\varphi} = (\hbar/4eB_{so,\varphi})^{1/2}$ are plotted in Figs. 4(b) and 4(d),

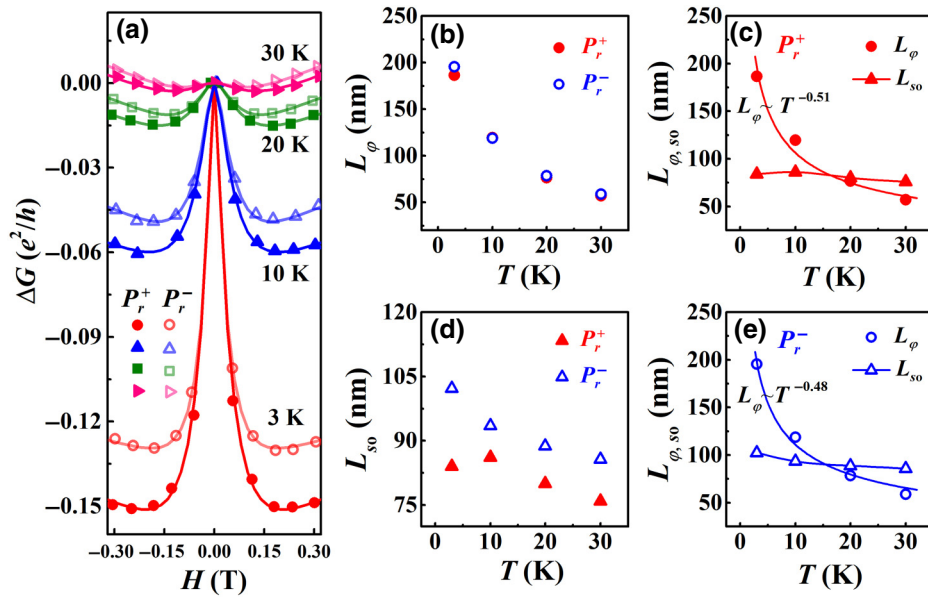


FIG. 4. (a) Low-field magnetoconductance, $\Delta G(e^2/h)$, of the 75-nm $\text{Bi}_2\text{O}_2\text{Se}$ film for the P_r^+ and P_r^- states at different fixed temperatures. Solid lines represent the fitting results obtained with the HLN equation. (b) Dephasing length (L_φ) and (d) spin-relaxation length (L_{so}) as a function of temperature, extracted from $\Delta G(e^2/h)$ data for the P_r^+ and P_r^- states. Characteristic L_{so} and L_φ involved in WAL and WL as a function of temperature for (c) P_r^+ and (e) P_r^- states, and, especially, solid lines for L_φ in (c),(e) are fits to experimental data by the power function.

respectively. L_φ shows almost no dependence on the polarization state [Figs. 4(b)] and basically follows a power law of $L_\varphi \sim T^{-0.5}$ [Figs. 4(c) and 4(e)]. This indicates that the dephasing process is primarily due to Nyquist scattering, i.e., electron-electron scattering with small energy transfers [37,38]. In contrast, L_{so} presents a clear polarization-induced difference [Fig. 4(d)], which is attributed to the modulation of the carrier density by the ferroelectric field effect. The values of $L_{so} \sim 84$ nm for the P_r^+ state and about 102 nm for the P_r^- state at 3 K—shorter than about 290 nm in $\text{Al}_x\text{Ga}_{1-x}\text{N}/\text{GaN}$ 2DEG and about 250 nm in InSb nanowires—prove the presence of a strong SOI in the $\text{Bi}_2\text{O}_2\text{Se}$ film [39,40]. Here, because of the inherent inversion symmetry present in $\text{Bi}_2\text{O}_2\text{Se}$, and given the electric-field-induced polarization charges, therefore, the Rashba-type SOI is the most likely dominant mechanism in the 2D $\text{Bi}_2\text{O}_2\text{Se}$ film, consistent with previous reports [41,42]. Remarkably, the polarization-induced controllability of L_{so} is much stronger than the conventional dielectric gating effect in $\text{Bi}_2\text{O}_2\text{Se}$ nanoplates [33]. These results significantly demonstrate ferroelectric gating control of the SOI in the $\text{Bi}_2\text{O}_2\text{Se}/\text{PMN-PT}$ system.

Furthermore, L_{so} and L_φ for the P_r^+ and P_r^- states are, respectively, plotted in Figs. 4(c) and 4(e) and show a crossover with increasing temperature. This nicely illustrates the key aspect that, when the L_{so} is shorter than L_φ for $T < 15$ K, the WAL is observed because spin precession destroys the phase coherence of the electron-wave

function on the time-reversed closed path; otherwise, the WL is dominant due to a thermally enhanced dephasing process [43]. As the carrier density for the P_r^+ state is higher than that for the P_r^- state for the 75-nm film [Fig. 2(a)], this results in shorter L_{so} and larger L_φ/L_{so} for the P_r^+ state, which gives rise to the stronger WAL, as manifested by the sharper negative ΔG in Fig. 4(a). All these analyses fully prove that the WAL effect and Rashba-type SOI in the $\text{Bi}_2\text{O}_2\text{Se}$ film can be nonvolatilely manipulated by switching the ferroelectric polarization.

The thickness-dependent magnetoconductance, ΔG , of the $\text{Bi}_2\text{O}_2\text{Se}$ films with thicknesses ranging from 75 to 150 nm at 3 K is shown in Fig. 5(a). All theoretical fittings with HLN theory to experimental data are in good agreement. As the films become thicker, the characteristic WAL peak around zero magnetic field is gradually weakened, presenting a thickness-dependent WAL-WL crossover. Moreover, the derived spin-relaxation length, L_{so} ; dephasing length, L_φ ; and mean free path, L_{el} , basically decrease with increasing film thickness (Fig. S12 within the Supplemental Material [24]). As a result, L_φ gradually approaches L_{so} in thicker films, leading to a neglectable WAL effect in the 150-nm film [Fig. 5(a)]. This is also reflected by the intersection point between L_{so} and L_φ shifting to lower temperature with increasing film thickness [Figs. 4(c) and 4(e) and Figs. S10 and S11 within the Supplemental Material [24]]. Thus, the stronger WAL effect and more-effective manipulation of the SOI through the ferroelectric field effect is expected in the

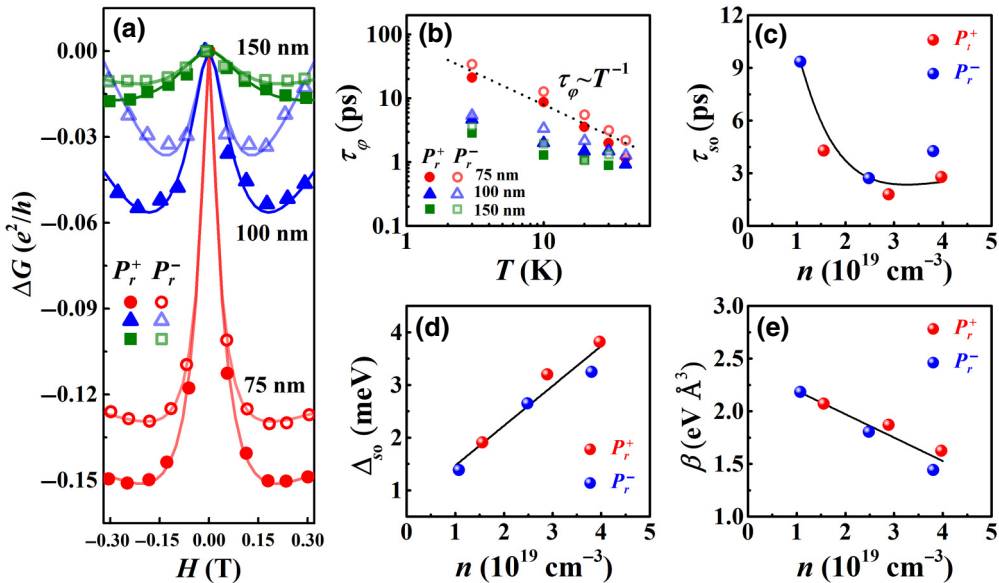


FIG. 5. (a) Magnetoconductance of $\text{Bi}_2\text{O}_2\text{Se}$ films with different thicknesses for the P_r^+ and P_r^- states of PMN-PT. Solid lines show fittings of experimental data with the HLN equation. (b) Temperature dependence of phase-relaxation time, τ_φ , of $\text{Bi}_2\text{O}_2\text{Se}$ films with different thicknesses; dotted line signifies $\tau_\varphi \sim T^{-1}$ for Nyquist dephasing. (c) Spin-relaxation time, τ_{so} , as a function of carrier density; line is a guide to the eye. (d) Variation of spin-orbit splitting energy, Δ_{so} , with volume carrier density, n . (e) Carrier-density-dependent Rashba coefficient, β . Solid lines in (d),(e) are linear fits to data.

thinner $\text{Bi}_2\text{O}_2\text{Se}$ film, the carrier density of which can be more effectively modulated by ferroelectric polarization.

Significantly, the influences of the ferroelectric field effect on the phase and spin-relaxation times are further elaborated. The phase-relaxation time can be obtained by $\tau_\varphi = \hbar/(4eDB_\varphi)$, where the diffusion coefficient, $D = v_F^2 \tau_{\text{tr}}/2$, is calculated from the Fermi velocity, $v_F = k_F \hbar/m^*$, and transport relaxation time $\tau_{\text{tr}} = \mu m^*/e$ with a Fermi wave vector of $k_F = (3\pi n)^{1/3}$ and an effective electron mass of $m^* = 0.184m_e$. As shown in Fig. 5(b), the temperature dependence of τ_φ scales as $\tau_\varphi \sim T^{-1}$, which can provide evidence again that Nyquist dephasing with the electron-electron interaction is the main phase-relaxation mechanism [37]. However, for thicker $\text{Bi}_2\text{O}_2\text{Se}$ films, the variation trend of τ_φ versus T diverges from the dotted line about T^{-1} , which may originate from the deviation from the 2D nature. On the other hand, the spin-relaxation time, τ_{so} , is given by $\tau_{so} = \hbar/(4eDB_{so})$. Taking the 75-nm film as an example, this yields a spin-relaxation time of $\tau_{so} \sim 9$ ps for the P_r^- state, which is much larger than that of $\tau_{so} \sim 4$ ps for the P_r^+ state (Table I), due to the stronger SOI in the higher-carrier-density state [33,37].

Again, this result demonstrates the polarization-induced tunability of the SOI upon switching the polarization state from P_r^- to P_r^+ .

Given that the Rashba SOI contributes to band-spin splitting, the corresponding spin-splitting energy is calculated using $\Delta_{so} = \hbar/(2\tau_{\text{tr}} \tau_{so})^{1/2}$. The carrier-density-dependent Δ_{so} plotted in Fig. 5(d) shows that Δ_{so} increases linearly with the carrier density for $\text{Bi}_2\text{O}_2\text{Se}$ films with different thicknesses. This also supports that the dominant SOI mechanism is the Rashba type [36]. Therefore, the Rashba coefficient, β , for the SOI can be further obtained from $4\beta^2 k_F^6 = \Delta_{so}^2 = (2e\hbar D/\tau_{\text{tr}})B_{so}$. The calculated value of β presents a systematic variation trend in relation to the carrier density [Fig. 5(e)], similar to some systems, like 2DEG in SrTiO_3 FETs or the 2D hole gas in gated diamond devices [35,38]. Notably, the values of Δ_{so} derived here, e.g., 1.3–1.9 meV for the 75-nm $\text{Bi}_2\text{O}_2\text{Se}$ film (Table I), exceed many other 2D systems in terms of magnitude [44,45]. More impressively, the nonvolatile modulation of Δ_{so} realized here through ferroelectric polarization is intrinsically different from the volatile one after removing the electric field from dielectric gates.

TABLE I. The values of transport parameters and SOI-related parameters for 75-nm film at 3 K.

| | n (cm^{-3}) | μ ($\text{cm}^2 \text{V}^{-1} \text{s}^{-1}$) | D ($\text{m}^2 \text{s}^{-1}$) | L_{so} (nm) | L_φ (nm) | τ_{so} (ps) | Δ_{so} (meV) | β ($\text{eV} \text{\AA}^3$) |
|---------|--------------------------|---|------------------------------------|---------------|------------------|------------------|---------------------|--------------------------------------|
| P_r^+ | 1.56×10^{19} | 133.33 | 0.0017 | 84.0 | 186.4 | 4.29 | 1.91 | 2.07 |
| P_r^- | 1.07×10^{19} | 115.95 | 0.0011 | 102.2 | 195.4 | 9.35 | 1.38 | 2.18 |

IV. CONCLUSIONS

In the present work, 2D Bi₂O₂Se films are epitaxially grown on ferroelectric PMN-PT (001) substrates to form Bi₂O₂Se/PMN-PT 2D FEFETs. The *in situ* electric field control of the carrier density, resistance, and magnetoresistance are realized by the ferroelectric field effect. Furthermore, the polarization state, film thickness, and temperature-dependent WAL effect are systematically measured and analyzed. The low-field magnetoconductance of the WAL with HLN fittings demonstrates the presence of a strong spin-orbit interaction in 2D Bi₂O₂Se films due to the asymmetric confinement potential. The crossover of the WAL to the WL is primarily determined by the relative scale of the spin-relaxation length and the dephasing length, and the main phase-relaxation mechanism is Nyquist scattering. Remarkably, the modulation of the spin-orbit interaction realized by ferroelectric gating is reversible and nonvolatile. Our work manifests that heterostructured systems utilizing films with the Rashba SOI and ferroelectric polarization can achieve reversible and nonvolatile manipulation of the SOI, which may inspire schemes for spintronics and related quantum applications.

ACKNOWLEDGMENTS

This work is supported by the National Natural Science Foundation of China (Grant No. 11974155). X.W. and W.Z. acknowledge support from the ARC Centre of Excellence in Future Low-Energy Electronics Technologies (Grant No. CE170100039).

- [1] K. C. Nowack, F. H. L. Koppens, Y. V. Nazarov, and M. K. Vandersypen, Coherent control of a single electron spin with electric fields, *Science* **318**, 1430 (2007).
- [2] A. Manchon, H. C. Koo, J. Nitta, S. M. Frolov, and R. A. Duine, New perspectives for Rashba spin-orbit coupling, *Nat. Mater.* **14**, 871 (2015).
- [3] W. Desrat, F. Giazotto, V. Pellegrini, M. Governale, and F. Beltram, Anticrossings of spin-split Landau levels in an InAs two-dimensional electron gas with spin-orbit coupling, *Phys. Rev. B* **71**, 153314 (2005).
- [4] G. Dresselhaus, Spin-orbit coupling effects in zinc blende structures, *Phys. Rev.* **100**, 580 (1955).
- [5] Y. A. Bychkov and E. I. Rashba, Oscillatory effects and the magnetic susceptibility of carriers in inversion layers, *J. Phys. C* **17**, 6039 (1984).
- [6] A. T. Neal, H. Liu, J. Gu, and P. D. Ye, Magneto-transport in MoS₂: Phase coherence, spin orbit scattering and the Hall factor, *ACS Nano* **7**, 7077 (2013).
- [7] N. Hemsworth, V. Tayari, F. Telesio, S. Xiang, S. Roddaro, M. Caporali, A. Ienco, M. Serrano-Ruiz, M. Peruzzini, G. Gervais, T. Szkopek, and S. Heun, Dephasing in strongly anisotropic black phosphorus, *Phys. Rev. B* **94**, 245404 (2016).
- [8] E. Zhang, R. Chen, C. Huang, J. H. Yu, K. T. Zhang, W. Y. Wang, S. S. Liu, J. W. Ling, X. G. Wan, H. Z. Lu, and F. X. Xiu, Tunable positive to negative magnetoresistance in atomically thin WTe₂, *Nano Lett.* **17**, 878 (2017).
- [9] J. M. Yan, Z. X. Xu, T. W. Chen, M. Xu, C. Zhang, X. W. Zhao, F. Liu, L. Guo, S. Y. Yan, G. Y. Gao, F. F. Wang, J. X. Zhang, S. N. Dong, X. G. Li, H. S. Luo, W. Y. Zhao, and R. K. Zheng, Nonvolatile and reversible ferroelectric control of electronic properties of Bi₂Te₃ topological insulator thin films grown on Pb(Mg_{1/3}Nb_{2/3})O₃-PbTiO₃ single crystals, *ACS Appl. Mater. Interfaces* **11**, 9548 (2019).
- [10] Q. X. Zhu, M. M. Yang, M. Zheng, R. K. Zheng, L. J. Guo, Y. Wang, J. X. Zhang, X. M. Li, H. S. Luo, and X. G. Li, Ultrahigh tunability of room temperature electronic transport and ferromagnetism in dilute magnetic semiconductor and PMN-PT single-crystal-based field effect transistors via electric charge mediation, *Adv. Funct. Mater.* **25**, 1111 (2015).
- [11] M. Y. Yan, J. M. Yan, M. Y. Zhang, T. W. Chen, G. Y. Gao, F. F. Wang, Y. Chai, and R. K. Zheng, Nonvolatile manipulation of electronic and ferromagnetic properties of NiO-Ni epitaxial film by ferroelectric polarization charge, *Appl. Phys. Lett.* **117**, 232901 (2020).
- [12] D. Pantel, S. Goetze, D. Hesse, and M. Alexe, Reversible electrical switching of spin polarization in multiferroic tunnel junctions, *Nat. Mater.* **11**, 289 (2012).
- [13] D. Sun, M. Fang, X. Xu, L. Jiang, H. Guo, Y. Wang, W. Yang, L. Yin, P. C. Snijders, and T. Z. Ward, Active control of magnetoresistance of organic spin valves using ferroelectricity, *Nat. Commun.* **5**, 4396 (2014).
- [14] W. Lin, W. N. Lin, S. D. Pollard, R. Guo, Herng Y. Yoong, S. H. Chen, H. Wang, L. Liu, C. J. Li, X. J. Yu, J. X. Xiao, X. Chi, J. H. Yu, J. Zhou, T. J. Zhou, H. Yang, and J. S. Chen, Tuning of current-induced effective magnetic field through Rashba effect engineering in hybrid multiferroic structures, *NPG Asia Mater.* **10**, 740 (2018).
- [15] K. Cai, M. Yang, H. Ju, S. Wang, Y. Ji, B. Li, K. W. Edmonds, Y. Sheng, B. Zhang, N. Zhang, S. Liu, H. Zheng, and K. Wang, Electric field control of deterministic current-induced magnetization switching in a hybrid ferromagnetic/ferroelectric structure, *Nat. Mater.* **16**, 712 (2017).
- [16] N. Paul, T. Felix, V. A. Luis M, B. Julien, C. V. Diogo, G. Vincent, F. Stéphane, B. Agnès, V. Laurent, B. Manuel, and A. Jean-Philippe, Non-volatile electric control of spin-charge conversion in a SrTiO₃ Rashba system, *Nature* **580**, 483 (2020).
- [17] J. X. Wu, Y. J. Liu, Z. J. Tan, C. W. Tan, J. B. Yin, T. R. Li, T. Tu, and H. L. Peng, Chemical patterning of high-mobility semiconducting 2D Bi₂O₂Se crystals for integrated optoelectronic devices, *Adv. Mater.* **29**, 1704060 (2017).
- [18] J. X. Wu, C. W. Tan, Z. J. Tan, Y. J. Liu, J. B. Yin, W. H. Dang, M. Z. Wang, and H. L. Peng, Controlled synthesis of high-mobility atomically thin bismuth oxyselenide crystals, *Nano Lett.* **17**, 3021 (2017).
- [19] J. X. Wu, H. T. Yuan, M. M. Meng, C. Chen, Y. Sun, Z. Y. Chen, W. H. Dang, C. W. Tan, Y. J. Liu, J. B. Yin,

- Y. B. Zhou, S. Y. Huang, H. Q. Xu, Y. Cui, H. Y. Hang, Z. F. Liu, Y. L. Chen, B. H. Yan, and H. L. Peng, High electron mobility and quantum oscillations in non-encapsulated ultrathin semiconducting $\text{Bi}_2\text{O}_2\text{Se}$, *Nat. Nanotechnol.* **12**, 530 (2017).
- [20] Y. Liang, Y. J. Chen, Y. W. Sun, S. P. Xu, J. X. Wu, C. W. Tan, X. F. Xu, H. T. Yuan, L. X. Yang, Y. L. Chen, P. Gao, J. D. Guo, and H. L. Peng, Molecular beam epitaxy and electronic structure of atomically thin oxyselenide films, *Adv. Mater.* **31**, 1901964 (2019).
- [21] Y. Y. Lv, L. Xu, S. T. Dong, Y. C. Luo, Y. Y. Zhang, Y. B. Chen, S. H. Yao, J. Zhou, Y. S. Cui, S. T. Zhang, M. H. Lu, and Y. F. Chen, Electron-electron scattering dominated electrical and magnetotransport properties in the quasi-two-dimensional Fermi liquid single-crystal $\text{Bi}_2\text{O}_2\text{Se}$, *Phys. Rev. B* **99**, 195143 (2019).
- [22] X. W. Zhao, S. N. Dong, G. Y. Gao, Z. X. Xu, M. Xu, J. M. Yan, W. Y. Zhao, Y. K. Liu, S. Y. Yan, J. X. Zhang, Y. Wang, H. Z. Lu, X. G. Li, J. K. Furdyna, H. S. Luo, and R. K. Zheng, Reversible and nonvolatile manipulation of the electronic transport properties of topological insulators by ferroelectric polarization switching, *npj Quantum Mater.* **3**, 52 (2018).
- [23] M. Fang, Ya. M. Wang, H. Wang, Y. S. Hou, E. Vetter, Y. F. Kou, W. T. Yang, L. F. Yin, Z. Xiao, Z. Li, L. Jiang, H. N. Lee, S. F. Zhang, R. Q. Wu, X. S. Xu, D. L. Sun, and J. Shen, Tuning the interfacial spin-orbit coupling with ferroelectricity, *Nat. Commun.* **11**, 2627 (2020).
- [24] See the Supplemental Material at <http://link.aps.org/supplemental/10.1103/PhysRevApplied.18.044073> for fitting of ILP theory; the low-field magnetoconductance fitted with HLN and ILP theory; schematic configuration of R and Hall measurements; the RC taken on the $\text{Bi}_2\text{O}_2\text{Se}$ (004) diffraction peak; the backscattered electron image and elemental mapping of Bi, O, and Se elements taken on the 75-nm $\text{Bi}_2\text{O}_2\text{Se}$ film; the AFM image of the 100-nm $\text{Bi}_2\text{O}_2\text{Se}$ film and out-of-plane PFM images of different polarization states of a PMN-PT substrate; the $\Delta R/R$ with 75, 100, and 150 nm as a function of electric field, E , applied to PMN-PT substrates; temperature dependence of the Hall mobility of $\text{Bi}_2\text{O}_2\text{Se}$ films with different thicknesses for the P_r^+ and P_r^- states of PMN-PT; the MR of different thicknesses of $\text{Bi}_2\text{O}_2\text{Se}$ film for P_r^+ and P_r^- states of PMN-PT at different temperatures; WAL effect in the 100- and 150-nm $\text{Bi}_2\text{O}_2\text{Se}$ film spin; and L_ϕ , L_{so} , and L_{el} as a function of temperature of $\text{Bi}_2\text{O}_2\text{Se}$ films with different thicknesses for the P_r^+ and P_r^- states of PMN-PT.
- [25] Z. X. Xu, J. M. Yan, M. Xu, L. Guo, T. W. Chen, G. Y. Gao, S. N. Dong, M. Zheng, J. X. Zhang, Y. Wang, X. G. Li, H. S. Luo, and R. K. Zheng, Integration of oxide semiconductor thin films with relaxor-based ferroelectric single crystals with large reversible and nonvolatile modulation of electronic properties, *ACS Appl. Mater. Interfaces* **10**, 32809 (2018).
- [26] G. Bergmann, Weak localization in thin films, *Phys. Rep.* **107**, 1 (1984).
- [27] J. Liao, Y. Ou, X. Feng, S. Yang, C. Lin, W. Yang, K. Wu, K. He, X. Ma, Q. K. Xue, and Y. Li, Observation of Anderson Localization in Ultrathin Films of Three-Dimensional Topological Insulators, *Phys. Rev. Lett.* **114**, 216601 (2015).
- [28] Q. Y. Xu, L. Hartmann, H. Schmidt, H. Hochmuth, M. Lorenz, R. S. Grund, C. Sturm, D. Spemann, and M. Grundmann, Metal-insulator transition in Co-doped ZnO: Magnetotransport properties, *Phys. Rev. B* **73**, 205342 (2006).
- [29] Q. Y. Xu, L. Hartmann, H. Schmidt, H. Hochmuth, M. Lorenz, and D. Spemann, s - d exchange interaction induced magnetoresistance in magnetic ZnO, *Phys. Rev. B* **76**, 134417 (2007).
- [30] R. Wang, R. S. Deacon, J. Yao, C. M. Lieber, and K. Ishibashi, Electrical modulation of weak antilocalization and spin-orbit interaction in dual gated Ge/Si core/shell nanowires, *Semicond. Sci. Technol.* **32**, 094002 (2017).
- [31] S. Hikami, A. I. Larkin, and Y. Nagaoka, Spin-orbit interaction and magnetoresistance in the two-dimensional random system, *Prog. Theor. Phys.* **63**, 707 (1980).
- [32] S. V. Iordanskii, Y. B. Lyanda-Geller, and G. E. Pikus, Weak localization in quantum wells with spin-orbit interaction, *JETP Lett.* **60**, 206 (1994).
- [33] M. M. Meng, S. Y. Huang, C. W. Tan, J. X. Wu, Y. M. Jing, H. L. Peng, and H. Q. Xu, Strong spin-orbit interaction and magnetotransport in semiconductor $\text{Bi}_2\text{O}_2\text{Se}$ nanoplates, *Nanoscale* **10**, 2704 (2018).
- [34] Z. Y. Chen, H. T. Yuan, Y. F. Zhang, K. Nomura, T. Gao, Y. B. Gao, H. Shimotani, Z. F. Liu, and Y. Iwasa, Tunable spin-orbit interaction in trilayer graphene exemplified in electric-double-layer transistors, *Nano Lett.* **12**, 2212 (2012).
- [35] H. Nakamura, T. Koga, and T. Kimura, Experimental Evidence of Cubic Rashba Effect in an Inversion-Symmetric Oxide, *Phys. Rev. Lett.* **108**, 206601 (2012).
- [36] V. Sazgari, G. Sullivan, and I. I. Kaya, Interaction-induced crossover between weak antilocalization and weak localization in a disordered InAs/GaSb double quantum well, *Phys. Rev. B* **101**, 155302 (2020).
- [37] C. Niu, G. Qiu, Y. X. Wang, Z. C. Zhang, M. W. Si, W. Z. Wu, and P. D. Ye, Gate-tunable strong spin-orbit interaction in two-dimensional tellurium probed by weak antilocalization, *Phys. Rev. B* **101**, 205414 (2020).
- [38] G. Akhgar, O. Klochan, L. Beveren, M. T. Edmonds, F. Maier, B. J. Spencer, J. C. McCallum, L. Ley, A. R. Hamilton, and C. I. Pakes, Strong and tunable spin-orbit coupling in a two-dimensional hole gas in ionic-liquid gated diamond devices, *Nano Lett.* **16**, 3768 (2016).
- [39] N. Thillosen, S. Cabanas, N. Kaluza, V. A. Guzenko, H. Hardtdegen, and T. Schapers, Weak antilocalization in gate-controlled $\text{Al}_x\text{Ga}_{1-x}\text{N}/\text{GaN}$ two-dimensional electron gases, *Phys. Rev. B* **73**, 241311 (2006).
- [40] I. vanWeperen, B. Tarasinski, D. Eeltink, V. S. Pribiag, S. R. Plissard, E. P. A. M. Bakkers, L. P. Kouwenhoven, and M. Wimmer, Spin-orbit interaction in InSb nanowires, *Phys. Rev. B* **91**, 201413 (2015).
- [41] J. Ying, J. He, G. Yang, M. Liu, Z. Lv, X. Zhang, H. Liu, K. Zhao, R. Jiang, Z. Ji, J. Fan, C. Yang, X. Jing, G. Liu, X. Cao, X. Wang, L. Lu, and F. Qu, Magnitude and spatial distribution control of the supercurrent in $\text{Bi}_2\text{O}_2\text{Se}$ -based Josephson junction, *Nano Lett.* **20**, 2569 (2020).

- [42] S. V. Eremeev, Y. M. Koroteev, and E. V. Chulkov, Surface electronic structure of bismuth oxychalcogenides, [Phys. Rev. B](#) **100**, 115417 (2019).
- [43] H. Yuan, M. S. Bahramy, and B. J. Yang, Zeeman-type spin splitting controlled by an electric field, [Nat. Phys.](#) **9**, 563 (2013).
- [44] G. M. Minkov, A. A. Sherstobitov, A. V. Germanenko, O. E. Rut, V. A. Larionova, and B. N. Zvonkov, Antilocalization and spin-orbit coupling in the hole gas in strained GaAs/In_xGa_{1-x}As/GaAs quantum well heterostructures, [Phys. Rev. B](#) **71**, 165312 (2005).
- [45] R. Moriya, K. Sawano, Y. Hoshi, S. Masubuchi, Y. Shiraki, A. Wild, C. Neumann, G. Abstreiter, D. Bougeard, T. Koga, and T. Machida, Cubic Rashba Spin-Orbit Interaction of a Two-Dimensional Hole Gas in a Strained-Ge/SiGe Quantum Well, [Phys. Rev. Lett.](#) **113**, 086601 (2014).